ACS APPLIED MATERIALS & INTERFACES

www.acsami.org

Research Article

In Situ Probing of Mass Exchange at the Solid Electrolyte Interphase in Aqueous and Nonaqueous Zn Electrolytes with EQCM-D

Saida Cora, Suzalmurni Ahmad, and Niya Sa*

Cite This: *ACS Appl. Mater. Interfaces* 2021, 13, 10131−10140

Read Online

ACCESS | Metrics & More | Article Recommendations | Supporting Information

ABSTRACT: Multivalent chemistry provides intriguing benefits of developing beyond lithium ion energy storage technologies and has drawn extensive research interests. Among the multivalent candidates, metallic zinc anodes offer an attractive high volumetric capacity at a low cost for designing the secondary ion batteries. However, the interfacial mass exchange at the Zn electrolyte/anode boundary is complicated. The least understood solid electrolyte interphase (SEI) occurs simultaneously with the reversible metal deposition, and its dynamic progression is unclear and difficult to capture. One major challenge to investigate such a dynamic interface is the lack of *in situ* analytical methods that offer direct mass transport information to reproduce the realistic battery operating conditions in an air-sensitive, nonaqueous electrolyte environment with a high *iR* drop. Work reported here reveals an in-depth analysis of the complex and dynamic SEI at the Zn electrolyte/electrode interface utilizing a multiharmonic quartz crystal microbalance with a dissipation method combined with the spectroscopic analysis. Key differences are observed for the SEI formation in the nonaqueous $Zn(TFSI)_2$ electrolyte in contrast to the aqueous $ZnCl_2$ electrolyte for reversible Zn deposition. A large disproportional loss of coulombs relative to the gravimetric mass change is prominently observed at the initial electrochemical cycles in the nonaqueous Zn electrolyte, and results suggest an *in situ* formation of an ionically permeable SEI layer that is compositionally featured with a rich content of organic S and N components. Further overtone-dependent dissipation analysis implies the changes in viscoelasticity at the electrode interface during the early SEI formation in the nonaqueous $Zn(TFSI)_2$ electrolyte.

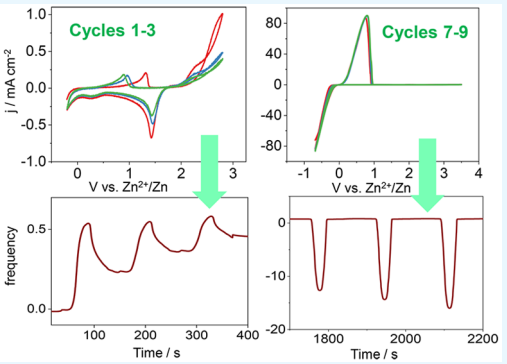

KEYWORDS: *multivalent batteries, solid electrolyte interphase, zinc ion battery, Zn electrolyte, in situ Zn deposition, EQCM with dissipation*

1. INTRODUCTION

Multivalent ion batteries offer an innovative potential low-cost energy storage strategy with bringing new concepts of a multistep electron transfer process per redox reaction. If successful, such batteries would yield leaping breakthroughs with improved energy density at a lower cost while utilizing abundant elements in contrast to the state-of-art lithium ion batteries that currently dominate in the electric vehicle market.[1−4] Among the promising multivalent systems, Zn-ion batteries have been enthusiastically studied because of its low cost, high volumetric capacity (5845 mAh/cm^3), and promising stability.[5−10] Rechargeable Zn ion batteries with compatibility of Zn metal anode are particularly promising;[11−13] for instance, the highly reversible MnO_2 cathode system with an aqueous Zn electrolyte has been recently reported to achieve over 5000 cycles with a capacity retention of 92%.[14−17] Although the greatly reversible Zn deposition in aqueous Zn system is quite attractive,[18] its application is limited by hydrogen evolution which results in a lower cutoff voltage for cell operation.[19−21] Therefore, considerable research efforts have been diverged to exploring the non-aqueous electrolyte candidates for reversible Zn plating[22−26] and to realize possible solid-state Zn ion conduction compounds.[27,28] Despite the promising features of the multivalent Zn system, one prominent challenge arises from the complexity of the nonaqueous Zn electrolyte is its least understood electrode/electrolyte interface, which directly leads to the mysterious instability issues of the Zn cells. It has been reported that the Zn ion battery functioning with a nonaqueous $Zn(TFSI)_2$ electrolyte requisites an electrochemical preconditioning process to stabilize the battery interfaces to maintain a stable capacity.[29,30] In addition, the battery suffers from a concurrent decline of the open circuit voltage upon cycling attributed from the self-discharge of the Zn anode, possibly ascribed from unwanted Zn dissolution.[31]

Received: January 10, 2021
Accepted: February 8, 2021
Published: February 17, 2021

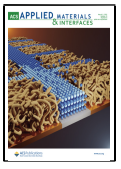

More recently, Nazar's team reported a high-capacity Zn cathode composed of layered $V_3O_7{\cdot}H_2O$ that showed remarkable Zn^{2+} storage in an aqueous Zn electrolyte with a Zn metal anode. Such a cell owns the capability of delivering a high specific capacity of over 300 mAh/g at high current rates. However, the same $V_3O_7{\cdot}H_2O$ cathode displayed a poor performance in the nonaqueous Zn electrolyte, with only one-third Zn ion intercalation in contrast to a two Zn ion intercalation in the aqueous electrolyte. In addition, a lowered current rate and a large activation energy are associated with the nonaqueous Zn electrolyte.[32] One major cause of the poor electrochemical performance is due to the complicated desolvation penalty associated with the Zn cation at its interface.[32] Other reported studies related to Zn full cells with the nonaqueous Zn electrolytes exhibited similar diminishing of the battery's capacity.[33] Despite the recent advances in the development of the next generation Zn ion batteries, a comprehensive understanding of the interfacial mass transport at the solid Zn and the liquid electrolyte junction is lacking in the literature.

Essential battery chemistry happens at the interface, where the exchange of electrons via redox reactions at the electrode surface dictates cell characteristics such as the operation voltage and capacity of the battery. These processes are complex and difficult to investigate with merely current based measurements, such as cyclic voltammetry. Furthermore, redox reactions can be hindered by the formation of complicated surface known as solid electrolyte interphase (SEI).[34−41] Formation and stability of the dynamic SEI are critical for preventing the continuous consumption of electrolyte and rapid capacity fade.[42,43] Characterization of the *in situ* SEI formation is essential to shed light on the mechanism of reversible Zn deposition and to evaluate the electrolyte role to the SEI formation.[44] Such understanding is hindered by the lack of adequate analytical methods with capabilities to perform the *in situ* mass transport characterization at the interface. Research work reported here is geared toward understanding the fundamental mass transport for the complex interfacial evolution in the multivalent Zn systems. The larger picture of this work is to draw a close parallel comparison between the mass transfer versus the charge transfer reactions occurring at the electrolyte-dependent Zn metal anode interface to understand the SEI evolution. The goal is to provide qualitative and quantitative analysis to understand possible SEI formation mechanisms and evaluate the long-term stability and cyclability of the multivalent Zn system. Herein, real-time characterizations for reversible deposition at Zn metal anode interface are investigated in the aqueous $ZnCl_2$ (zinc chloride) and nonaqueous $Zn(TFSI)_2$ (zinc bis(trifluoromethanesulfonyl)imide) electrolytes as case studies, with the *in situ* multifold electrochemical quartz crystal microbalance with dissipation (EQCM-D) analysis combined with the FTIR spectroscopic analysis. Key notable differences are observed between the aqueous versus the nonaqueous Zn electrolyte for reversible Zn deposition, where the aqueous $ZnCl_2$ electrolyte exhibits reversible electrochemical and mass transport property evident from the overlaps in cyclic voltammetry and a reproducible mass change upon reversible Zn electrodeposition. By contrast, the nonaqueous $Zn(TFSI)_2$ system shows complex interfacial reactions at initial electrochemical cycles where a disproportional consumption of coulombs is noted with no significant change of the gravimetric mass. Findings from the spectroscopic analysis indicate SEI upon electrochemical cycling for the $Zn(TFSI)_2$ electrolyte results in the formation of an ionically permeable layer. In addition, an overtone-dependent frequency and dissipation response at the initial electrochemical cycles in the nonaqueous electrolyte further signifies an inhomogeneous SEI formation at the interface. Results suggest a completely different SEI formation mechanism for an aqueous $ZnCl_2$ versus a nonaqueous $Zn(TFSI)_2$ electrolyte, and the qualitative and quantitative findings about SEI in this work offer useful guidelines for energy storage communities for designing stable interfaces.

2. EXPERIMENTAL SECTION

Materials and Electrolyte Preparation. Zinc(II) bis(trifluoromethanesulfonyl)imide (99.5%, Solvionic) was dried overnight (at 130 °C, <100 mTorr) in a vacuum oven located in an argon-filled glovebox with H_2O and O_2 under 0.1 ppm. Acetonitrile (99.9%, anhydrous, Acros Organics) solvent was pretreated overnight with dried molecular sieve (Aldrich, 3 Å beads, 4−8 mesh) for 24 h before use. The salt was then added to the anhydrous acetonitrile and mixed until completely dissolved to prepare a 0.2 M $Zn(TFSI)_2$ electrolyte. All nonaqueous electrolyte preparations were performed under an inert atmosphere in the argon-filled glovebox. High purity zinc chloride (99.999%, Sigma-Aldrich) and deionized water (Millipore-Q, 18.2 MΩ·cm) were used to prepare a 0.2 M aqueous $ZnCl_2$ electrolyte.

Electrochemical Measurements. Electrochemical quartz crystal microbalance measurements were performed with the quartz crystal microbalance instrument (Q-Sense from Biolin scientific) located in the argon-filled glovebox (Vacuum Technology Inc.) with H_2O and O_2 under 0.1 ppm. The measurements were conducted by using an in-home designed electrochemical *in situ* cell coupled with the quartz crystal microbalance with dissipation (EQCM-D) chamber. The resonators were 5.0 MHz AT-cut quartz crystals precoated with gold (14.0 mm in diameter, Biolin). Zinc metal (99.9%, Goodfellow) was mechanically polished and served as both reference and counter electrodes in the electrochemical flow cell. The EQCM-D resonator was used as the working electrode to realize the frequency and the electrochemical measurements simultaneously. Before introduction of the electrolyte into the chamber, the sensor was stabilized, and the baseline frequency and dissipation curves were collected. The frequency measurements were obtained with odd overtones at n = 3, 5, 7, and 9. Electrochemical impedance spectroscopy (EIS) was applied in the frequency range of 0.05 Hz−1 MHz for the aqueous $ZnCl_2$ electrolyte and 0.1 Hz−1 MHz for the nonaqueous $Zn(TFSI)_2$ electrolyte. For the 0.2 M $ZnCl_2$ electrolyte the analysis was performed for 23 electrochemical cycles with EIS measured at the 3rd, 13th, and 23rd electrochemical cycles. For the 0.2 M $Zn(TFSI)_2$ electrolyte the analysis was performed for 12 cycles with EIS monitoring at the 3rd, 6th, 9th, and 12th electrochemical cycles. The data acquisition for EQCM-D measurements was performed by using QSoft software. Data acquisition from the electrochemical measurements was performed by using VersaStudio.

FTIR Analysis. Surface characterization of the cycled electrodes was performed by using a Nicolet iS50 Fourier transform infrared absorption spectrometer (FTIR) equipped with an attenuated total reflectance (ATR) detector. FTIR spectral data were collected by performing 64 scans with spectral resolution of 8 cm^{-1} in the range between 4000 and 400 cm^{-1}. The resonator electrode serving as the working electrode was cycled in the electrolyte solution referenced with Zn metal and then separated from the cell for FTIR characterization. The cycled electrode was mounted directly on the ATR stage and tightly clamped. For the 0.2 M aqueous $ZnCl_2$ electrolyte, the spectral data were collected and compared on the resonator electrode after one electrochemical cycle versus after 20 consecutive electrochemical cycles, where the potential window is scanned from 0.8 to −0.5 V at a scan rate of 0.05 V/s. For the 0.2 M $Zn(TFSI)_2$ in ACN electrolyte, spectral data were collected and compared on the resonator electrode for one electrochemical cycle

https://dx.doi.org/10.1021/acsami.1c00565
ACS Appl. Mater. Interfaces 2021, 13, 10131−10140

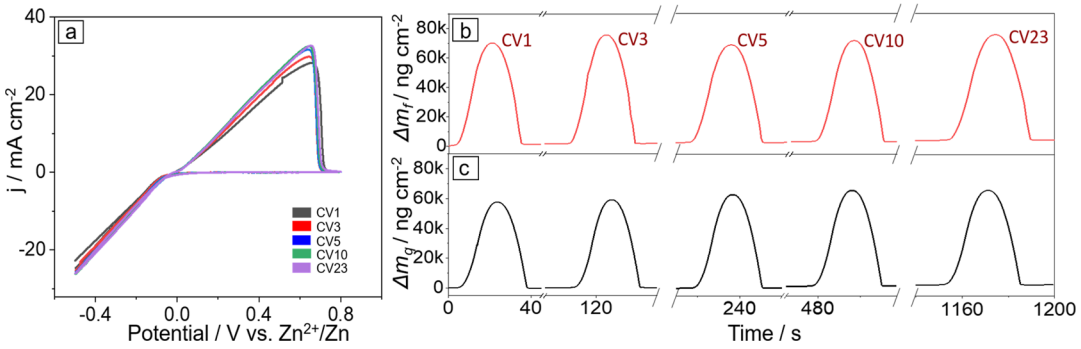

Figure 1. (a) Cyclic voltammograms of reversible Zn deposition in a 0.2 M $ZnCl_2$ aqueous electrolyte. A three-electrode cell is used with Au-coated resonator as working electrode and Zn metal as reference and counter electrodes with representative CVs at the 1st, 3rd, 5th, 10th, and 23rd electrochemical cycles. The scan rate is 0.05 V/s. (b) EQCM-D frequency determined gravimetric mass Δm_f (red) at the resonator (n = 3). (c) Faradaic mass change Δm_q (black) at the corresponding CV cycles.

versus for 11 consecutive electrochemical cycles, with the potential scanned from 2.5 to −1.0 V at a scan rate of 0.05 V/s. Data collection and spectral calculations were performed by using OMNIC software.

3. RESULTS AND DISCUSSION

The multiharmonic EQCM-D technique presented in this work holds two unique features that are different from a conventional EQCM operated with the fundamental resonance. First, the multiharmonics mode with the overtone measurements (n = 1, 3, 5, 7, and 9) offers a complex frequency response that correlates various penetration depths with the homogeneity of the interface through probing the transverse wave of a resonator. Second, quantification of the dissipation factor provides information that directly links hydrodynamic properties with viscoelastic changes at the interface.[45−49] Therefore, the multiharmonic EQCM-D opens a new path of capturing the dynamic mass transport properties at the nonstationary solid electrolyte interphase.

Mass transport of continuous electrochemical deposition of Zn from a 0.2 M aqueous $ZnCl_2$ electrolyte is compared in parallel with a nonaqueous 0.2 M $Zn(TFSI)_2$ electrolyte in acetonitrile. It is worth noting that $ZnCl_2$ is selected as the representative aqueous electrolyte candidate because of its acceptable solubility in water, facile kinetics, and future potentials to be applied to the next-generation rechargeable Zn ion battery systems.[6,50,51] Upon electrochemical cycling, rigid Zn mass gain and loss are quantified by the frequency change of the quartz resonator. The change in frequency is proportional to the mass loss or gain attributed to the charge transfer reactions at the interface. Without taking into consideration the surface adsorption effect, the rigid mass load Δm_f is ascribed to the inertial mass rigidly attached at the resonator and is proportional to the frequency change, Δf_{mass}, as described by the Sauerbrey equation:

$$\Delta m_f = -\frac{\sqrt{\rho_q \mu_q}}{2f_0^2}(\Delta f/n) = -C(\Delta f/n) \quad (1)$$

where f_0 is the fundamental frequency of the quartz crystal, ρ_q is the specific density of the resonator (2.648 g/cm^3),[52] μ_q is the shear modulus of quartz (2.947×10^{11} g/(cm·s^2)),[52] C is the sensitivity constant 17.7 ng/(cm^2·Hz),[53] and n is the overtone order. On the other hand, the faradaic contribution to the mass change defined as Δm_q can be determined by integrating the faradaic current, as presented in eq 2

$$\Delta m_q = \frac{M_{Zn}\int_0^t i\,dt}{2F} \quad (2)$$

where M_{Zn}, i, t, and F represent molecular mass of Zn, faradaic current, time, and faradaic constant, respectively. The simplest aqueous $ZnCl_2$ electrolyte is investigated as a proof of concept with *in situ* EQCM-D to probe the fundamental mass transport evolution upon continuous electrochemical cycling for reversible Zn deposition. A home-built *in situ* electrochemical cell is constructed to represent the confined and inert environment for the rechargeable ion battery. The Au-coated quartz resonator is used as a working electrode with Zn metal as reference and counter electrodes. The initial inflow of the electrolyte solution and the adsorption effect on the electrode surface are excluded with the assumption of the water solvent being a Newtonian liquid with sufficiently low viscosity. The changes of the frequency and dissipation at overtones are collected simultaneously in the same time domain with the electrochemical cycles. Cyclic voltammetry is conducted at the potential window from −0.5 to 0.8 V at a scan rate of 0.05 V/s. Zn electrodeposition is initiated at −0.06 V while Zn dissolution starts at 0.02 V, giving a 0.08 V overpotential. Representative CV cycles are presented in Figure 1a. The corresponding characteristic mass exchange at the interface with differences in gravimetric mass (Δm_f) measured from the frequency change of the resonator as determined by eq 1 and the faradaic mass (Δm_q) determined by eq 2 at continuous CV cycles are reported in Figure 1b,c. Representative Δm_f is shown for the electrochemical cycles 1, 3, 5, 10, and 23 (Figure 1b). The gravimetric mass change per electrochemical cycle across a series of continuous 23 CV cycles gives a discrepancy of <1.7% on average, with an average coulombic efficiency of ∼99.9%, indicating a near-complete and reversible Zn deposition and dissolution for the aqueous $ZnCl_2$ electrolyte (CE versus cycle numbers is shown in Figure S1a).

In contrast, a 0.2 M $Zn(TFSI)_2$ electrolyte in acetonitrile is used as a case study for the nonaqueous electrolyte to investigate the interfacial mass transport at continuous electrochemical cycles. It is worth mentioning that it is of great interest to the energy storage community to explore such a TFSI anion based nonaqueous Zn electrolyte due to its promising opportunities in rechargeable energy storage applications.[54−58] Interestingly, no obvious reversible Zn deposition is observed during the initial three CV scans for the $Zn(TFSI)_2$ electrolyte. Apparent reversible Zn deposition

https://dx.doi.org/10.1021/acsami.1c00565
ACS Appl. Mater. Interfaces 2021, 13, 10131−10140

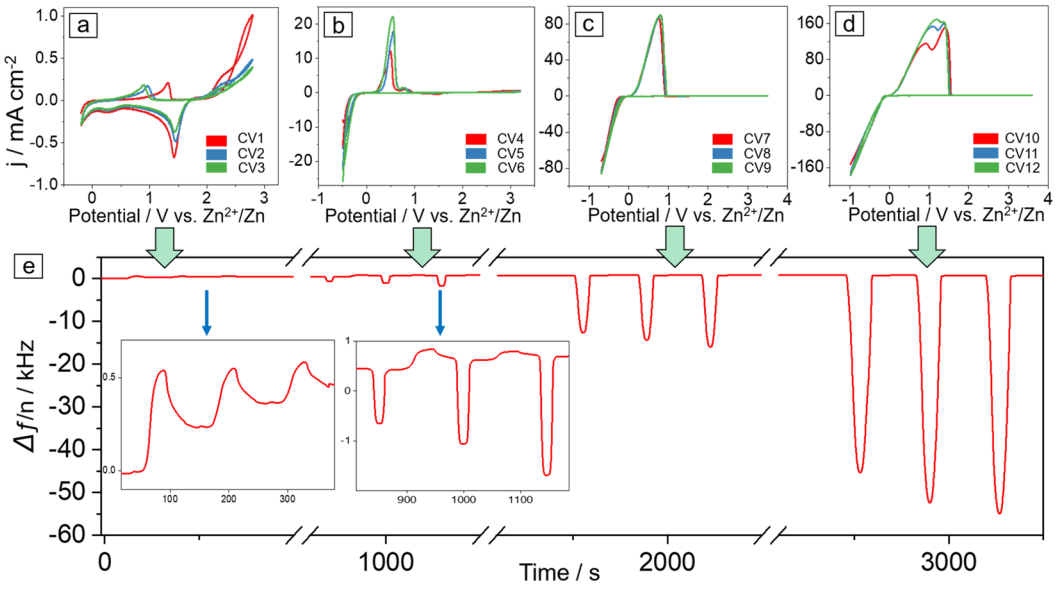

Figure 2. (a–d) Cycling voltammograms of reversible Zn deposition for a 0.2 M $Zn(TFSI)_2$ in acetonitrile. A three-electrode cell is used with Au-coated resonator as the working electrode, and Zn metal is used as the reference and counter electrodes. The scan rate is 0.05 V/s. Each panel represents three consecutive CV cycles (from the 1st CV to the 12th CV cycle). The voltage window is scanned from 2.8 to −0.2 V for CV1–3, 3.2 to −0.5 V for CV4–6, 3.5 to −0.7 V for CV7–9, and 3.6 to −1.0 V for CV10–12. (e) Corresponding frequency changes measured from the EQCM-D at the resonator (n = 3) for the 12 consecutive CV cycles (the two enlarged windows represent the frequency changes for CV1–3 and CV4–6).

is not seen until the continuous electrochemical cycling at the fourth CV scan, as presented in Figure 2 where simultaneous frequency change of the resonator corresponding to each CV scan is shown. Reversible Zn deposition reported for further electrochemical cycles from the 4th to the 12th cycle gives an average coulombic efficiency of ∼99.9% (CE from cycle to cycle is shown in Figure S1b). The initial three electrochemical cycles are the essence of the SEI formation process where the SEI layer is well adhered to the electrode, and this layer prevents further electrolyte decomposition and maintains the further cycling performance to ensure the continued CV cycles with a up to 3.8 V oxidation limit for the $Zn(TFSI)_2$/ACN electrolyte. This is consistent with Han's report where the electrolyte oxidation of $Zn(TFSI)_2$/ACN is reported to be ∼3.8 V.[22] This conclusion is also further evidenced in the literature for Zn anodes where the charge transfer resistance was significantly decreased after the initial electrochemical cycle, signifying the presence of the SEI at the initial electrochemical cycles.[23] Detailed electrochemistry, frequency, and dissipation analyses are presented in the following sections.

The essence of the coulomb loss is investigated with the goal to understand the dynamic evolution of SEI and possible layer formation mechanism at the interface. The mass deviation ratio ($\Delta M\%$), defined as the ratio of the mass difference taken from the gravimetric mass Δm_f (eq 1) and the faradaic mass Δm_q (eq 2) to the theoretical mass loss or gain, is illustrated in eq 3. In theory, a rigid mass deposition that is a completely faradaic process shall give a mass deviation ratio of zero, indicating that the mass sensed from the frequency change is in 100% agreement with the mass transport from the Zn/Zn^{2+} redox chemistry, and this reference point is presented in the dashed line in Figure 3.

$$\Delta M\% = \frac{\Delta m_f - \Delta m_q}{\Delta m_q} \times 100\% \tag{3}$$

A cycle-to-cycle comparison of $\Delta M\%$ calculated from the aqueous $ZnCl_2$ electrolyte (Figure 3a) versus the nonaqueous

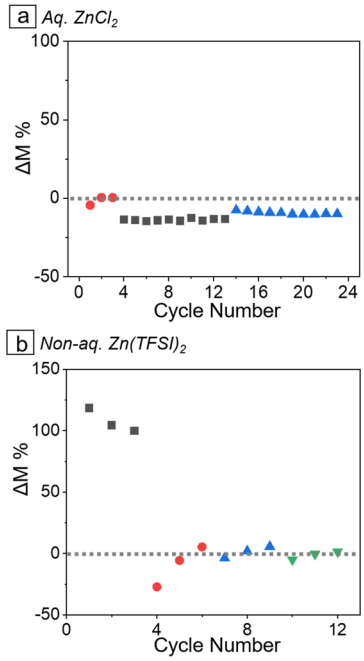

Figure 3. Mass deviation ratio ($\Delta M\%$) versus cycle number representing the mass difference between the Sauerbrey mass and faradaic mass for (a) a 0.2 M aqueous $ZnCl_2$ electrolyte and (b) a 0.2 M nonaqueous $Zn(TFSI)_2$ electrolyte in acetonitrile. The gray dashed line represents the reference line where the mass deviation ratio is zero.

https://dx.doi.org/10.1021/acsami.1c00565
ACS Appl. Mater. Interfaces 2021, 13, 10131–10140

$Zn(TFSI)_2$ electrolyte (Figure 3b) presents substantial difference at initial electrochemical cycles. For the aqueous $ZnCl_2$ electrolyte, the average mass discrepancy $\Delta M\%$ is found to be ~1.7% for cycle 1 to cycle 3 with the average $\Delta M\%$ increasing to ~13.7% for the continued cycles (cycle 4 to 13). $\Delta M\%$ decreases and stabilizes to ~9.4% for further cycles (cycle 14 to 23). For the aqueous $ZnCl_2$, $\Delta M\%$ is ascribed to the hydrodynamic correction assigned to the trapped mobile liquid with the electrode particles as well as the surface roughness of the electrode which consequently contributes to the frequency change.[45] A similar observation is discussed and explained explicitly in Aurbach's paper utilizing a standard electrochemical Cu deposition model where the intrinsically porous electrode surface is the major contributor to the discrepancy in frequency and dissipation between cycles.[59] To our surprise, the above finding is rather different for the nonaqueous $Zn(TFSI)_2$ system where a large $\Delta M\%$ is presented at the early electrochemical cycles with a significant mass discrepancy of Δm_f to Δm_q observed. The average $\Delta M\%$ is 107% at the initial three electrochemical cycles, indicating a large loss of coulombs without contributing to the Zn mass gain. A less prominent but noteworthy $\Delta M\%$ of 27% is observed at cycle 4, which is significantly higher than the aqueous Zn system. For further electrochemical cycles from cycle 5 to cycle 12, a stabilized mass discrepancy of about 3.6% on average is observed, which is comparable to the aqueous $ZnCl_2$ system. The significant loss of coulombs for the nonaqueous $Zn(TFSI)_2$ system, especially at its initial electrochemical cycles, suggests the presence of complicated interfacial reactions in parallel with the electrolyte redox reactions. Two factors mainly contribute to such large mass discrepancy ($\Delta M\%$): (1) possible formation of soluble solid electrolyte interphase and reaction intermediates, accompanied by the solvent/electrolyte redox reactions that consume charge that contributes to current, and (2) complicated interfacial reactions that are conspicuously occurring during the initial cycling without an immediate nucleation and growth of Zn metal upon electrochemical cycling.[33,60] Consequently, the initial mass change for the $Zn(TFSI)_2$ system does not entirely follow the rigid model, and the Sauerbrey correlation is not precise enough to quantify the mass change for the film formation. As a result, the change of the viscoelastic nature at the interface convolutes the rigid mass determined from the Sauerbrey equation.

To better explore the loss of coulombs and the SEI nature at the initial CV cycles for the $Zn(TFSI)_2$ electrolyte, simultaneous cyclic voltammetry is presented in parallel with the chronoamperometry data and the frequency shift of the resonator at the same time domain in Figure 4. Cyclic voltammetry at the first cycle suggests prominent cathodic current peaks at 1.4 V (Figure 4c). The anodic current peak is seen at 1.3 V at the first CV cycle, and it shifts to 0.96 V at the second cycle and 0.88 V at the third cycle (first CV scan is shown in Figure 4c; second and third CV scans are in Figure S6). This redox feature could possibly be ascribed to the electro-hydrodimerization process of acetonitrile, resulting in the formation of the enamine products.[61,62] For the continued second and third CV cycles, the electrolyzed solution loses its anodic feature at ~2.1 V, an indication of the ligand oxidation reaction for the formation of the intermediate products.[63,64] Subsequently, the solvent redox reactions at the initial three CV scans result in a positive frequency shift and directly lead to a negative Sauerbrey mass. Such a mass difference is an

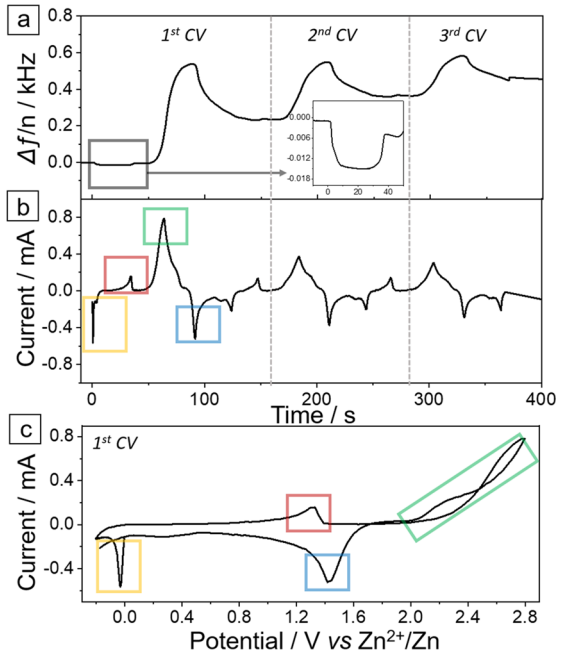

Figure 4. EQCM-D of the initial three electrochemical cycles for a 0.2 M nonaqueous $Zn(TFSI)_2$ in acetonitrile electrolyte. (a) Frequency change versus time at the resonator electrode at the 3rd overtone.; (b) Current versus time profile. (c) The first CV cycle for the nonaqueous $Zn(TFSI)_2$ electrodeposition performed in the three-electrode cell with Au EQCM-D resonator serving as a working electrode and Zn metal as both reference and counter electrodes. The voltage window is scanned from 2.8 to −0.2 V against Zn metal reference electrode at a scan rate of 0.05 V/s.

indication of the punctual load mass contribution at the interface ascribed from a radical-surface reactivity of an adhered film formation, which consequently leads to a typical softening process at the interface.[47,65,66] A continuous increase of the frequency baseline observed at the initial three CV cycles offers further evidence for the possibility of such film formation, which is attributed to the radical reactions and the consumption of the coulombs. The difference between the baseline frequency from cycle to cycle reaches a constant level beyond the fifth electrochemical cycle. Results from the frequency shift suggest such initial film formation is a dynamic process with an increase of the film thickness upon the initial electrochemical cycling.

Fourier transform infrared spectroscopy (FTIR) characterization offers insights into the chemical features of the SEI and was performed at the interface for the representative aqueous $ZnCl_2$ and nonaqueous $Zn(TFSI)_2$ electrolytes. For the *in situ* SEI formation in the $Zn(TFSI)_2$ electrolyte, the mass deviation ratio ($\Delta M\%$) ascribed from the loss of coulombs, which occurred at the early electrochemical cycles, is recognized as the major contributor to the SEI formation. FTIR spectroscopic analysis showed that the electrode interface after 11 electrochemical cycles in the $Zn(TFSI)_2$ electrolyte is enriched with organic functional groups in comparison with the interface after one electrochemical cycle as presented in Figure 5a,b. Findings suggest an *in situ* formation of an ionically permeable SEI layer that compositionally featured with a rich content of organic S and N components as evidenced by the intensified peaks of S−O (1566, 1441, 1350−1138, and 700−500 cm^{-1}), S−N (1350−1138, 797, and 745 cm^{-1}), C−F (1350−1138 and 700−500 cm^{-1}), and C−S−N (700−500

https://dx.doi.org/10.1021/acsami.1c00565
ACS Appl. Mater. Interfaces 2021, 13, 10131−10140

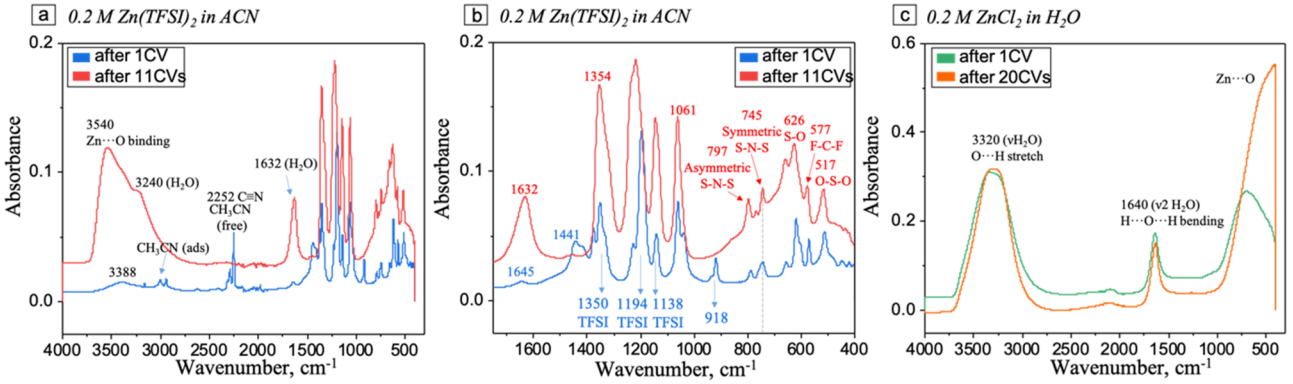

Figure 5. FTIR spectra of electrochemically cycled EQCM-D resonator: (a) in a 0.2 M $Zn(TFSI)_2$/ACN electrolyte after 1 CV (blue) cycle and after 11 CVs (red) cycles with wavenumbers from 4000 to 400 cm^{-1}; (b) enlarged FTIR spectra of (a) with wavenumbers from 1750 to 400 cm^{-1}; (c) in a 0.2 M $ZnCl_2/H_2O$ electrolyte after 1 CV (green) cycle and after 20 CVs (orange) cycles with wavenumbers from 4000 to 400 cm^{-1}.

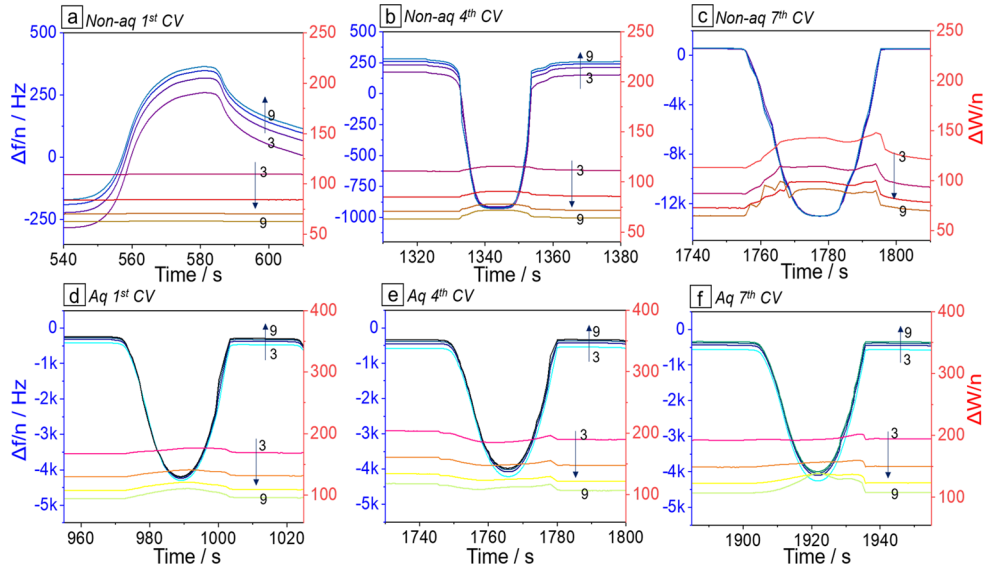

Figure 6. Frequency and dissipation changes at different overtones, n (= 3, 5, 7, and 9), as a function of time during the 1st, 4th, and 7th CV cycles for (a–c) a 0.2 M nonaqueous $Zn(TFSI)_2$ electrolyte and (d–f) a 0.2 M aqueous $ZnCl_2$ electrolyte. The direction of the arrow indicates the increase of the overtone order from n = 3 to 9.

cm^{-1}) upon electrochemical cycling, and such layer composition has been reported to be permeable for ion transfer.[57] In addition, the spectrum is highly sensitive to the presence of H_2O, and continuous electrochemical cycling gives rise to strong absorption peaks at around 3400 and 1600 cm^{-1}. The spectroscopic analysis is supported by the EQCM-D results where a continuous increase of the frequency change along the initial electrochemical cycles proved SEI growth. This SEI coating stabilizes and sustains the continuous electrochemistry cycling for the nonaqueous $Zn(TFSI)_2$/ACN, which leads to a stabilized CE.

For the *in situ* SEI formation in the $ZnCl_2$ electrolyte, the 3320 cm^{-1} peak corresponds to the O–H stretching due to the presence of water molecules bound to the surface of anode and the 1640 cm^{-1} peak represents an overtone of the H_2O molecule. A prominent increase of the absorption <700 cm^{-1}, known as the fingerprint region of ZnO, is observed at the anode interface upon 20 electrochemical cycles as compared with the electrode surface upon one electrochemical cycle; for instance, the sharp absorption band located at 429 cm^{-1} is indicative of the Zn···O vibrational band from ZnO_2 or ZnO.[67−69] The proposed mechanism of SEI formation in aqueous Zn electrolyte is that trace Zn oxidation occurs along Zn plating, which results in the formation of soluble $Zn(OH)_4^{2-}$, which further decomposes into ZnO and H_2O. While the Zn stripping process is accompanied by the simultaneous parasitic reaction of hydrogen evolution,[70] the formation of the trace amount of porous Zn oxides stays at the interface at further electrochemical cycles, which is also verified by the *in situ* EQCM-D measurement where a mass layer is evidenced by a gradual negative drift of a baseline frequency (Figure S2).

Further analysis of the overtone-dependent dissipation change ($\Delta W/n$) relative to the frequency difference ($\Delta f/n$) is performed at three representative electrochemical cycles, the 1st, 4th, and 7th CV scans for both the aqueous $ZnCl_2$ and nonaqueous $Zn(TFSI)_2$ electrolytes, shown in Figure 6. Dissipation stays as a constant at different overtones for the nonaqueous $Zn(TFSI)_2$ electrolyte at its first electrochemical cycle, suggesting that the viscous dissipation at the electrode surface is essentially comparable across overtones. Because of the balance between the population changes of the ion adsorption and the solvent dimerization, the change of mass reflected in the change of frequency is observed without having

https://dx.doi.org/10.1021/acsami.1c00565
ACS Appl. Mater. Interfaces 2021, 13, 10131−10140

the redox chemistry of the Zn/Zn^{2+}. These results are in agreement with the findings from the electrochemical data which indicate that possible homogeneous radical reactions are instigated in a quasi-uniform manner. The characteristic pattern of the overtone (n)-dependent $\Delta f/n$ and $\Delta W/n$ is observed for the nonaqueous $Zn(TFSI)_2$ electrolyte at early electrochemical cycles (Figure 6a,b) and is reflected by a moderate increase of $\Delta f/n$ and a decrease of $\Delta W/n$ with n dependence. This phenomenon implies inhomogeneity of the SEI formation in the $Zn(TFSI)_2$ electrolyte and suggests changes in viscoelasticity at the electrode interface upon plating and stripping of Zn at initial electrochemical cycles. A less noteworthy overtone dependence of the frequency at the seventh CV (Figure 6c) and the later electrochemical cycles (cycles 8−12) (Figure S3) must be due to the retarded impregnation of the electrode interface with reversible and reproducible Zn deposition. Aqueous $ZnCl_2$, on the other hand, at its first CV cycle, shows a prominent shift of the frequency profile aligned with the gravimetric change for Zn plating and stripping (Figure 6d). The dissipation ($\Delta W/n$) increases by the end of the plating cycle and decreases by the end of the stripping cycle, which suggests a dimensional change at the electrode/electrolyte interface. The overtone-dependent dissipation implies cooperative desolvation and solvation of Zn for the stripping and plating process, respectively. In contrast, at the fourth CV cycle, the frequency profile for the aqueous $ZnCl_2$ electrolyte (Figure 6e) resembles a sinusoidal function in comparison with the square wave profile of the nonaqueous $Zn(TFSI)_2$ electrolyte (Figure 6b). Such a profile difference mainly suggests that a higher overpotential is required to initiate the Zn stripping process for the nonaqueous $Zn(TFSI)_2$ system as compared with $ZnCl_2$, indicating that the nonaqueous Zn stripping process is a relatively slow kinetic process versus the aqueous Zn stripping. This conclusion is further supported by evaluating the plating overpotential (η_α) and the stripping overpotential (η_β) (defined in Figure S4) for the $Zn(TFSI)_2$ and $ZnCl_2$ electrolytes in Figure 7. The enlarged overpotential in $Zn(TFSI)_2$ electrolyte upon cycling directly results in an increase of faradaic current and consequently leads to an increase of the frequency difference, suggesting growth of the mass gain (Figures 7 and 2e). Results suggest an increased thermodynamic driving force to initiate the Zn stripping process for the nonaqueous $Zn(TFSI)_2$ system, and the accompanied increase of the current density indicates a higher electromotive force is needed to remove the plated Zn or a higher desolvation energy is required for Zn stripping.

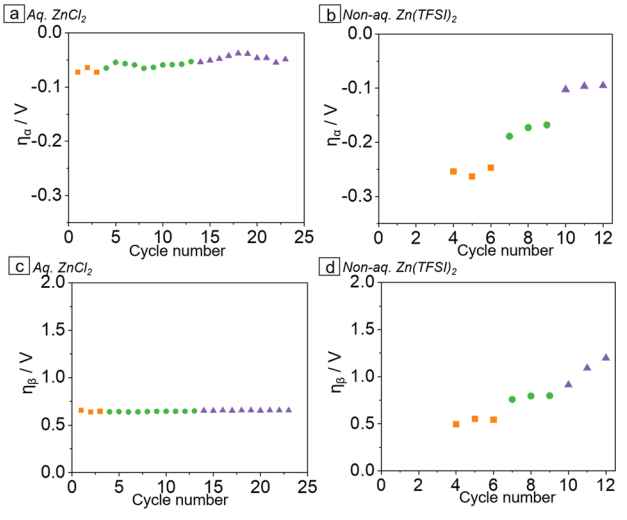

Figure 7. Plating overpotential (η_α) and stripping overpotential (η_β) versus cycle number. (a, b) η_α of a 0.2 M $ZnCl_2$ aqueous electrolyte and a 0.2 M $Zn(TFSI)_2$ in acetonitrile electrolyte. (c, d) η_β of a 0.2 M $ZnCl_2$ aqueous electrolyte and a 0.2 M $Zn(TFSI)_2$ in acetonitrile electrolyte.

4. CONCLUSION

In conclusion, the *in situ* SEI formation and the fundamental mass transport properties in the aqueous $ZnCl_2$ electrolyte and the nonaqueous $Zn(TFSI)_2$ electrolyte for reversible Zn deposition are investigated by simultaneous gravimetric measurement, FTIR analysis, and *in situ* hydrodynamic spectroscopic characterization. Several notable differences are examined. The apparent Zn deposition does not occur in $Zn(TFSI)_2$ during its initial electrochemical cycles, and a large consumption of charge is observed, causing a conspicuous discrepancy between gravimetric mass change versus faradaic mass change. Such a discrepancy becomes less prominent at further electrochemical cycles for $Zn(TFSI)_2$. In addition, an overtone-dependent frequency and dissipation of $Zn(TFSI)_2$ at its initial electrochemical cycles signify nonuniform changes in viscoelastic properties at the electrode interface. In contrast, the aqueous $ZnCl_2$ electrolyte does not show a "conditioning process" at its initial electrochemical cycles; therefore, no significant loss of charge occurs, resulting in a small overall discrepancy between gravimetric mass and faradaic mass for 23 continuous electrochemical cycles with nearly 100% CE. Despite the advances in the multivalent nonaqueous battery systems, there are still many challenges ahead. The fundamental investigation of the interfacial mass transport properties and SEI formation for Zn deposition can serve as a guideline to manipulate the SEI chemistry for the purpose of improving the performance and design of multivalent nonaqueous batteries.

■ ASSOCIATED CONTENT

Supporting Information

The Supporting Information is available free of charge at https://pubs.acs.org/doi/10.1021/acsami.1c00565.

Additional electrochemical, SEM and EQCM-D data (PDF)

■ AUTHOR INFORMATION

Corresponding Author

Niya Sa − *Department of Chemistry, University of Massachusetts Boston, Boston, Massachusetts 02125, United States;* orcid.org/0000-0003-4656-5851; Email: Niya.Sa@umb.edu

Authors

Saida Cora − *Department of Chemistry, University of Massachusetts Boston, Boston, Massachusetts 02125, United States*

Suzalmurni Ahmad − *Department of Chemistry, University of Massachusetts Boston, Boston, Massachusetts 02125, United States*

Complete contact information is available at: https://pubs.acs.org/10.1021/acsami.1c00565

https://dx.doi.org/10.1021/acsami.1c00565
ACS Appl. Mater. Interfaces 2021, 13, 10131−10140

Author Contributions

N.S. led this project and performed the EQCM cell fabrication. S.C. performed EQCM-D characterization, data calculation, and analysis. S.A. helped with EIS characterization. N.S. led the data organization and writing with input from all listed authors. All authors have given an approval to the final version of the manuscript.

Funding

Financial support from research faculty startup funds, the Joseph P. Healey Research Grant, and the Endowed Faculty Career Development Award from University of Massachusetts Boston is acknowledged. Acquisition of the advanced FE-SEM is acknowledged from the MRI grant of the National Science Foundation (Grant No. 1919919).

Notes

The authors declare no competing financial interest.

■ ACKNOWLEDGMENTS

Financial support from research faculty startup funds, the Joseph P. Healey Research Grant, and the Endowed Faculty Carrer Development Award from University of Massachusetts Boston are acknowledged. Acquisition of the advanced FESEM is acknowledged from the MRI grant of the National Science Foundation (Grant No. 1919919). N.S. thanks Steve Shepard and support from the cleanroom of the Boston College Integrated Sciences.

■ REFERENCES

(1) Guduru, R. K.; Icaza, J. C. A Brief Review on Multivalent Intercalation Batteries with Aqueous Electrolytes. *Nanomaterials* **2016**, *6* (3), 41.

(2) Lapidus, S. H.; Rajput, N. N.; Qu, X. H.; Chapman, K. W.; Persson, K. A.; Chupas, P. J. Solvation Structure and Energetics of Electrolytes for Multivalent Energy Storage. *Phys. Chem. Chem. Phys.* **2014**, *16* (40), 21941−21945.

(3) Yuan, C. L.; Zhang, Y.; Pan, Y.; Liu, X. W.; Wang, G. L.; Cao, D. X. Investigation of the Intercalation of Polyvalent Cations (Mg2+, Zn2+) into lambda-MnO2 for Rechargeable Aqueous Battery. *Electrochim. Acta* **2014**, *116*, 404−412.

(4) Doe, R. E.; Han, R.; Hwang, J.; Gmitter, A. J.; Shterenberg, I.; Yoo, H. D.; Pour, N.; Aurbach, D. Novel, Electrolyte Solutions Comprising Fully Inorganic Salts with High Anodic Stability for Rechargeable Magnesium Batteries. *Chem. Commun.* **2014**, *50* (2), 243−245.

(5) Muldoon, J.; Bucur, C. B.; Gregory, T. Quest for Nonaqueous Multivalent Secondary Batteries: Magnesium and Beyond. *Chem. Rev.* **2014**, *114* (23), 11683−11720.

(6) Huang, S.; Zhu, J. C.; Tian, J. L.; Niu, Z. Q. Recent Progress in the Electrolytes of Aqueous Zinc-Ion Batteries. *Chem. - Eur. J.* **2019**, *25* (64), 14480−14494.

(7) Wang, F.; Hu, E. Y.; Sun, W.; Gao, T.; Ji, X.; Fan, X. L.; Han, F. D.; Yang, X. Q.; Xu, K.; Wang, C. S. A Rechargeable Aqueous Zn2+-Battery with High Power Density and a Long Cycle-Life. *Energy Environ. Sci.* **2018**, *11* (11), 3168−3175.

(8) Shen, C.; Li, X.; Li, N.; Xie, K. Y.; Wang, J. G.; Liu, X. R.; Wei, B. Q. Graphene-Boosted, High-Performance Aqueous Zn-Ion Battery. *ACS Appl. Mater. Interfaces* **2018**, *10* (30), 25446−25453.

(9) Blanc, L. E.; Kundu, D.; Nazar, L. F. Scientific Challenges for the Implementation of Zn-Ion Batteries. *Joule* **2020**, *4* (4), 771−799.

(10) Zhang, T.; Tang, Y.; Guo, S.; Cao, X.; Pan, A.; Fang, G.; Zhou, J.; Liang, S. Fundamentals and Perspectives in Developing Zinc-Ion Battery Electrolytes: a Comprehensive Review. *Energy Environ. Sci.* **2020**, *13*, 4625−4665.

(11) Tang, Y.; Liu, C. X.; Zhu, H. R.; Xie, X. S.; Gao, J. W.; Deng, C. B.; Han, M. M.; Liang, S. Q.; Zhou, J. Ion-Confinement Effect Enabled by Gel Electrolyte for Highly Reversible Dendrite-Free Zinc Metal Anode. *Energy Storage Mater.* **2020**, *27*, 109−116.

(12) Hao, J. N.; Li, X. L.; Zeng, X. H.; Li, D.; Mao, J. F.; Guo, Z. P. Deeply Understanding the Zn Anode Behaviour and Corresponding Improvement Strategies in Different Aqueous Zn-Based Batteries. *Energy Environ. Sci.* **2020**, *13* (11), 3917−3949.

(13) Wang, T.; Li, C.; Xie, X.; Lu, B.; He, Z.; Liang, S.; Zhou, J. Anode Materials for Aqueous Zinc Ion Batteries: Mechanisms, Properties, and Perspectives. *ACS Nano* **2020**, *14*, 16321−16347.

(14) Pan, H. L.; Shao, Y. Y.; Yan, P. F.; Cheng, Y. W.; Han, K. S.; Nie, Z. M.; Wang, C. M.; Yang, J. H.; Li, X. L.; Bhattacharya, P.; Mueller, K. T.; Liu, J. Reversible Aqueous Zinc/Manganese Oxide Energy Storage from Conversion Reactions. *Nat. Energy* **2016**, *1*, 16039.

(15) Sun, W.; Wang, F.; Hou, S. Y.; Yang, C. Y.; Fan, X. L.; Ma, Z. H.; Gao, T.; Han, F. D.; Hu, R. Z.; Zhu, M.; Wang, C. S. Zn/MnO2 Battery Chemistry With H+ and Zn2+ Coinsertion. *J. Am. Chem. Soc.* **2017**, *139* (29), 9775−9778.

(16) Xu, C. J.; Li, B. H.; Du, H. D.; Kang, F. Y. Energetic Zinc Ion Chemistry: The Rechargeable Zinc Ion Battery. *Angew. Chem., Int. Ed.* **2012**, *51* (4), 933−935.

(17) Wu, B. K.; Zhang, G. B.; Yan, M. Y.; Xiong, T. F.; He, P.; He, L.; Xu, X.; Mai, L. Q. Graphene Scroll-Coated alpha-MnO2 Nanowires as High-Performance Cathode Materials for Aqueous Zn-Ion Battery. *Small* **2018**, *14* (13), 1703850.

(18) Zeng, X. H.; Hao, J. N.; Wang, Z. J.; Mao, J. F.; Guo, Z. P. Recent Progress and Perspectives on Aqueous Zn-Based Rechargeable Batteries with Mild Aqueous Electrolytes. *Energy Storage Mater.* **2019**, *20*, 410−437.

(19) Desai, D.; Wei, X.; Steingart, D. A.; Banerjee, S. Electrodeposition of Preferentially Oriented Zinc for Flow-Assisted Alkaline Batteries. *J. Power Sources* **2014**, *256*, 145−152.

(20) Karami, H.; Mousavi, M. F.; Shamsipur, M. A Novel Dry Bipolar Rechargeable Battery Based on Polyaniline. *J. Power Sources* **2003**, *124* (1), 303−308.

(21) Trocoli, R.; La Mantia, F. An Aqueous Zinc-Ion Battery Based on Copper Hexacyanoferrate. *ChemSusChem* **2015**, *8* (3), 481−485.

(22) Han, S. D.; Rajput, N. N.; Qu, X. H.; Pan, B. F.; He, M. N.; Ferrandon, M. S.; Liao, C.; Persson, K. A.; Burrell, A. K. Origin of Electrochemical, Structural, and Transport Properties in Nonaqueous Zinc Electrolytes. *ACS Appl. Mater. Interfaces* **2016**, *8* (5), 3021−3031.

(23) Senguttuvan, P.; Han, S. D.; Kim, S.; Lipson, A. L.; Tepavcevic, S.; Fister, T. T.; Bloom, I. D.; Burrell, A. K.; Johnson, C. S. A High Power Rechargeable Nonaqueous Multivalent Zn/V2O5 Battery. *Adv. Energy Mater.* **2016**, *6* (24), 1600826.

(24) Chae, M. S.; Heo, J. W.; Kwak, H. H.; Lee, H.; Hong, S. T. Organic Electrolyte-Based Rechargeable Zinc-Ion Batteries Using Potassium Nickel Hexacyanoferrate as a Cathode Material. *J. Power Sources* **2017**, *337*, 204−211.

(25) Pan, C. S.; Nuzzo, R. G.; Gewirth, A. A. ZnAlxCo2-xO4 Spinels as Cathode Materials for Non-Aqueous Zn Batteries with an Open Circuit Voltage of ≤ 2 V. *Chem. Mater.* **2017**, *29* (21), 9351−9359.

(26) Dong, Y.; Di, S. L.; Zhang, F. B.; Bian, X.; Wang, Y. Y.; Xu, J. Z.; Wang, L. B.; Cheng, F. Y.; Zhang, N. Nonaqueous Electrolyte with Dual-Cations for High-Voltage and Long-Life Zinc Batteries. *J. Mater. Chem. A* **2020**, *8* (6), 3252−3261.

(27) Kundu, D.; Adams, B. D.; Duffort, V.; Vajargah, S. H.; Nazar, L. F. A High-Capacity and Long-Life Aqueous Rechargeable Zinc Battery Using a Metal Oxide Intercalation Cathode. *Nat. Energy* **2016**, *1*, 16119.

(28) Ta, K.; See, K. A.; Gewirth, A. A. Elucidating Zn and Mg Electrodeposition Mechanisms in Nonaqueous Electrolytes for Next-Generation Metal Batteries. *J. Phys. Chem. C* **2018**, *122* (25), 13790−13796.

(29) See, K. A.; Chapman, K. W.; Zhu, L. Y.; Wiaderek, K. M.; Borkiewicz, O. J.; Barile, C. J.; Chupas, P. J.; Gewirth, A. A. The Interplay of Al and Mg Speciation in Advanced Mg Battery Electrolyte Solutions. *J. Am. Chem. Soc.* **2016**, *138* (1), 328−337.

https://dx.doi.org/10.1021/acsami.1c00565
ACS Appl. Mater. Interfaces 2021, 13, 10131−10140

(30) Barile, C. J.; Nuzzo, R. G.; Gewirth, A. A. Exploring Salt and Solvent Effects in Chloride-Based Electrolytes for Magnesium Electrodeposition and Dissolution. *J. Phys. Chem. C* **2015**, *119* (24), 13524−13534.
(31) Guerfi, A.; Trottier, J.; Boyano, I.; De Meatza, I.; Blazquez, J. A.; Brewer, S.; Ryder, K. S.; Vijh, A.; Zaghib, K. High Cycling Stability of Zinc-Anode/Conducting Polymer Rechargeable Battery with Non-Aqueous Electrolyte. *J. Power Sources* **2014**, *248*, 1099−1104.
(32) Kundu, D.; Vajargah, S. H.; Wan, L. W.; Adams, B.; Prendergast, D.; Nazar, L. F. Aqueous vs. Nonaqueous Zn-Ion Batteries: Consequences of the Desolvation Penalty at the Interface. *Energy Environ. Sci.* **2018**, *11* (4), 881−892.
(33) Han, S. D.; Kim, S.; Li, D. G.; Petkov, V.; Yoo, H. D.; Phillips, P. J.; Wang, H.; Kim, J. J.; More, K. L.; Key, B.; Klie, R. F.; Cabana, J.; Stamenkovic, V. R.; Fister, T. T.; Markovic, N. M.; Burrell, A. K.; Tepavcevic, S.; Vaughey, J. T. Mechanism of Zn Insertion into Nanostructured delta-MnO2: A Nonaqueous Rechargeable Zn Metal Battery. *Chem. Mater.* **2017**, *29* (11), 4874−4884.
(34) Borodin, O.; Ren, X.; Vatamanu, J.; von Wald Cresce, A.; Knap, J.; Xu, K. Modeling Insight into Battery Electrolyte Electrochemical Stability and Interfacial Structure. *Acc. Chem. Res.* **2017**, *50* (12), 2886−2894.
(35) Agubra, V. A.; Fergus, J. W. The Formation and Stability of the Solid Electrolyte Interface on the Graphite Anode. *J. Power Sources* **2014**, *268*, 153−162.
(36) Bockelmann, M.; Becker, M.; Reining, L.; Kunz, U.; Turek, T. Passivation of Zinc Anodes in Alkaline Electrolyte: Part I. Determination of the Starting Point of Passive Film Formation. *J. Electrochem. Soc.* **2018**, *165* (13), A3048−A3055.
(37) Wang, L.; Menakath, A.; Han, F.; Wang, Y.; Zavalij, P. Y.; Gaskell, K. J.; Borodin, O.; Iuga, D.; Brown, S. P.; Wang, C.; Xu, K.; Eichhorn, B. W. Identifying the components of the Solid-Electrolyte Interphase in Li-Ion Batteries. *Nat. Chem.* **2019**, *11* (9), 789−796.
(38) Peled, E. The Electrochemical-Behavior of Alkali and Alkaline-Earth Metals in Non-Aqueous Battery Systems - the Solid Electrolyte Interphase Model. *J. Electrochem. Soc.* **1979**, *126* (12), 2047−2051.
(39) Verma, P.; Maire, P.; Novak, P. A Review of the Features and Analyses of the Solid Electrolyte Interphase in Li-Ion Batteries. *Electrochim. Acta* **2010**, *55* (22), 6332−6341.
(40) Winter, M. The Solid Electrolyte Interphase - The Most Important and the Least Understood Solid Electrolyte in Rechargeable Li Batteries. *Z. Phys. Chem.* **2009**, *223* (10−11), 1395−1406.
(41) Tripathi, A. M.; Su, W. N.; Hwang, B. J. In Situ Analytical Techniques for Battery Interface Analysis. *Chem. Soc. Rev.* **2018**, *47* (3), 736−851.
(42) Katorova, N. S.; Luchkin, S. Y.; Rupasov, D. P.; Abakumov, A. M.; Stevenson, K. J. Origins of Irreversible Capacity Loss in Hard Carbon Negative Electrodes for Potassium-Ion Batteries. *J. Chem. Phys.* **2020**, *152* (19), 194704.
(43) Luchkin, S. Y.; Lipovskikh, S. A.; Katorova, N. S.; Savina, A. A.; Abakumov, A. M.; Stevenson, K. J. Solid-Electrolyte Interphase Nucleation and Growth on Carbonaceous Negative Electrodes for Li-Ion Batteries Visualized with in Situ Atomic Force Microscopy. *Sci. Rep.* **2020**, *10* (1), 8550.
(44) Liu, T. C.; Lin, L. P.; Bi, X. X.; Tian, L. L.; Yang, K.; Liu, J. J.; Li, M. F.; Chen, Z. H.; Lu, J.; Amine, K.; Xu, K.; Pan, F. In Situ Quantification of Interphasial Chemistry in Li-Ion Battery. *Nat. Nanotechnol.* **2019**, *14* (1), 50−56.
(45) Levi, M. D.; Daikhin, L.; Aurbach, D.; Presser, V. Quartz Crystal Microbalance with Dissipation Monitoring (EQCM-D) for In-Situ Studies of Electrodes for Supercapacitors and Batteries: A Mini-Review. *Electrochem. Commun.* **2016**, *67*, 16−21.
(46) Levi, M. D.; Shpigel, N.; Sigalov, S.; Dargel, V.; Daikhin, L.; Aurbach, D. In Situ Porous Structure Characterization of Electrodes for Energy Storage and Conversion by EQCM-D: a Review. *Electrochim. Acta* **2017**, *232*, 271−284.
(47) Shpigel, N.; Levi, M. D.; Sigalov, S.; Girshevitz, O.; Aurbach, D.; Daikhin, L.; Jackel, N.; Presser, V. Non-Invasive In Situ Dynamic Monitoring of Elastic Properties of Composite Battery Electrodes by EQCM-D. *Angew. Chem., Int. Ed.* **2015**, *54* (42), 12353−12356.
(48) Yang, Z. Z.; Dixon, M. C.; Erck, R. A.; Trahey, L. Quantification of the Mass and Viscoelasticity of Interfacial Films on Tin Anodes Using EQCM-D. *ACS Appl. Mater. Interfaces* **2015**, *7* (48), 26585−26594.
(49) Shpigel, N.; Levi, M. D.; Aurbach, D. EQCM-D Technique for Complex Mechanical Characterization of Energy Storage Electrodes: Background and Practical Guide. *Energy Storage Mater.* **2019**, *21*, 399−413.
(50) Goh, F. W. T.; Liu, Z. L.; Hor, T. S. A.; Zhang, J.; Ge, X. M.; Zong, Y.; Yu, A. S.; Khoo, W. A Near-Neutral Chloride Electrolyte for Electrically Rechargeable Zinc-Air Batteries. *J. Electrochem. Soc.* **2014**, *161* (14), A2080−A2086.
(51) Zhang, L.; Rodriguez-Perez, I. A.; Jiang, H.; Zhang, C.; Leonard, D. P.; Guo, Q. B.; Wang, W. F.; Han, S. M.; Wang, L. M.; Ji, X. L. $ZnCl_2$ "Water-in-Salt" Electrolyte Transforms the Performance of Vanadium Oxide as a Zn Battery Cathode. *Adv. Funct. Mater.* **2019**, *29* (30), 1902653.
(52) Tsai, W. Y.; Taberna, P. L.; Simon, P. Electrochemical Quartz Crystal Microbalance (EQCM) Study of Ion Dynamics in Nanoporous Carbons. *J. Am. Chem. Soc.* **2014**, *136* (24), 8722−8728.
(53) Dargel, V.; Jäckel, N.; Shpigel, N.; Sigalov, S.; Levi, M. D.; Daikhin, L.; Presser, V.; Aurbach, D. In Situ Multilength-Scale Tracking of Dimensional and Viscoelastic Changes in Composite Battery Electrodes. *ACS Appl. Mater. Interfaces* **2017**, *9* (33), 27664−27675.
(54) Fan, S. Q.; Asselin, G. M.; Pan, B. F.; Wang, H.; Ren, Y.; Vaughey, J. T.; Sa, N. Y. A Simple Halogen-Free Magnesium Electrolyte for Reversible Magnesium Deposition through Cosolvent Assistance. *ACS Appl. Mater. Interfaces* **2020**, *12* (9), 10252−10260.
(55) Shterenberg, I.; Salama, M.; Yoo, H. D.; Gofer, Y.; Park, J. B.; Sun, Y. K.; Aurbach, D. Evaluation of $(CF_3SO_2)_2N^-$ (TFSI) Based Electrolyte Solutions for Mg Batteries. *J. Electrochem. Soc.* **2015**, *162* (13), A7118−A7128.
(56) Ha, S. Y.; Lee, Y. W.; Woo, S. W.; Koo, B.; Kim, J. S.; Cho, J.; Lee, K. T.; Choi, N. S. Magnesium(II) Bis(Trifluoromethane Sulfonyl)Imide-Based Electrolytes with Wide Electrochemical Windows for Rechargeable Magnesium Batteries. *ACS Appl. Mater. Interfaces* **2014**, *6* (6), 4063−4073.
(57) Qiu, H. Y.; Du, X. F.; Zhao, J. W.; Wang, Y. T.; Ju, J. W.; Chen, Z.; Hu, Z. L.; Yan, D. P.; Zhou, X. H.; Cui, G. L. Zinc Anode-Compatible In-Situ Solid Electrolyte Interphase via Cation Solvation Modulation. *Nat. Commun.* **2019**, *10* (1), 5374.
(58) Sa, N.; Rajput, N. N.; Wang, H.; Key, B.; Ferrandon, M.; Srinivasan, V.; Persson, K. A.; Burrell, A. K.; Vaughey, J. T. Concentration Dependent Electrochemical Properties and Structural Analysis of a Simple Magnesium Electrolyte: Magnesium Bis-(Trifluoromethane Sulfonyl)Imide in Diglyme. *RSC Adv.* **2016**, *6* (114), 113663−113670.
(59) Sigalov, S.; Shpigel, N.; Levi, M. D.; Feldberg, M.; Daikhin, L.; Aurbach, D. Electrochemical Quartz Crystal Microbalance with Dissipation Real-Time Hydrodynamic Spectroscopy of Porous Solids in Contact with Liquids. *Anal. Chem.* **2016**, *88* (20), 10151−10157.
(60) Zhang, N.; Dong, Y.; Wang, Y. Y.; Wang, Y. X.; Li, J. J.; Xu, J. Z.; Liu, Y. C.; Jiao, L. F.; Cheng, F. Y. Ultrafast Rechargeable Zinc Battery Based on High-Voltage Graphite Cathode and Stable Nonaqueous Electrolyte. *ACS Appl. Mater. Interfaces* **2019**, *11* (36), 32978−32986.
(61) Kurzweil, P.; Chwistek, M. Electrochemical Stability of Organic Electrolytes in Supercapacitors: Spectroscopy and Gas Analysis of Decomposition Products. *J. Power Sources* **2008**, *176* (2), 555−567.
(62) Masui, M.; Ueda, C.; Moriguchi, T.; Michida, T.; Kataoka, M.; Ohmori, H. Anodic Dimerization of Enamines, 2-Cyano-2-Phenylvinylamines. *Chem. Pharm. Bull.* **1984**, *32* (4), 1392−1400.
(63) Zhang, W. H.; Du, L. J.; Chen, Z. R.; Hong, J.; Yue, L. ZnO Nanocrystals as Anode Electrodes for Lithium-Ion Batteries. *J. Nanomater.* **2016**, *2016*, 1−7.

https://dx.doi.org/10.1021/acsami.1c00565
ACS Appl. Mater. Interfaces 2021, 13, 10131−10140

(64) Su, L. J.; Liu, L. Y.; Liu, B.; Meng, J. N.; Yan, X. B. Revealing the Impact of Oxygen Dissolved in Electrolytes on Aqueous Zinc-Ion Batteries. *Iscience* **2020**, *23* (4), 100995.
(65) Dargel, V.; Shpigel, N.; Sigalov, S.; Nayak, P.; Levi, M. D.; Daikhin, L.; Aurbach, D. In Situ Real-Time Gravimetric and Viscoelastic Probing of Surface Films Formation on Lithium Batteries Electrodes. *Nat. Commun.* **2017**, *8*, 1389.
(66) Castro, P.; Resa, P.; Elvira, L. Apparent Negative Mass in QCM Sensors Due to Punctual Rigid Loading. *IOP Conf. Ser.: Mater. Sci. Eng.* **2012**, *42*, 012046.
(67) Cheng, S.; Yan, D.; Chen, J. T.; Zhuo, R. F.; Feng, J. J.; Li, H. J.; Feng, H. T.; Yan, P. X. Soft-Template Synthesis and Characterization of ZnO2 and ZnO Hollow Spheres. *J. Phys. Chem. C* **2009**, *113* (31), 13630−13635.
(68) Bitenc, M.; Marinsek, M.; Orel, Z. C. Preparation and Characterization of Zinc Hydroxide Carbonate and Porous Zinc Oxide Particles. *J. Eur. Ceram. Soc.* **2008**, *28* (15), 2915−2921.
(69) Sreekantan, S.; Gee, L. R.; Lockman, Z. Room Temperature Anodic Deposition and Shape Control of One-Dimensional Nanostructured Zinc Oxide. *J. Alloys Compd.* **2009**, *476* (1−2), 513−518.
(70) Li, Y. G.; Dai, H. J. Recent Advances in Zinc-Air Batteries. *Chem. Soc. Rev.* **2014**, *43* (15), 5257−5275.

https://dx.doi.org/10.1021/acsami.1c00565
ACS Appl. Mater. Interfaces 2021, 13, 10131−10140